Linear-to-Dual-Circular Polarization Decomposition Metasurface Based on Rotated Trimming-Stub-Loaded Circular Patch

Tao Zhang [1,2], **Haoran Wang** [1,2], **Chongmei Peng** [1] **and Zhaohui Chen** [2,*]

[1] Institute of Microelectronics of the Chinese Academy of Sciences, Beijing 100029, China
[2] University of Chinese Academy of Sciences, Beijing 100049, China
* Correspondence: zhaohui.chen@sicm.com.cn

Abstract: This paper presents a linear-to-dual-circular polarization metasurface decomposer, which decomposes a linearly polarized (LP) planar incident wave into a pair of circular polarized (CP) waves, namely, a right-handed circular polarized (RHCP) wave and a left-handed circular polarized (LHCP) wave, and scatters them into different directions. The proposed metasurface polarization decomposer is composed of a series of rotated trimming stub loaded circular patches. The two CP components are excited due to the perturbation introduced by the trimming stubs, and the different phase gradients added to the RHCP and LHCP components are realized by rotating the circular patches with different angles. A 12×12 metasurface polarization decomposer is designed, fabricated, and measured, which scatters the RHCP and LHCP into $-30°$ and $30°$, respectively. The simulated and measured results agree well with each other, which demonstrates the proposed design.

Keywords: linear polarization; left-handed circular polarization; metasurface; polarization decomposer; right-handed polarization; trimming stubs

1. Introduction

Metasurfaces, the two-dimensional equivalent of voluminal three-dimensional metamaterials, have been becoming an emerging platform in manipulating electromagnetic waves, due to their natural benefits of low profiles, low costs, easy fabrications, and their flexible capabilities to electromagnetic wave transformations [1]. Metasurfaces have been widely applied in various fields, such as wavefront reshaping [2–4], frequency translation [5,6], wireless communication [7], holography [8,9], antenna performance enhancement [10,11], near-field focusing [12,13], energy absorption [14,15], electromagnetic nonreciprocity [16,17], etc.

Polarization state is a fundamental characteristic of electromagnetic waves, which is generally defined as the oscillating direction of their electrical waves. By controlling the polarization states of electromagnetic waves, a series of important applications have been reported, such as radar cross-section (RCS) reduction [18,19], information encryption [20,21], anti-jamming communication [22,23], and polarization multiplexing [24,25], to name a few.

Metasurfaces are also applied for controlling the polarization states of electromagnetic waves. Compared with conventional methods such as liquid crystals and solid crystals [26–28], which generally have bulky sizes and limited operating bandwidths, metasurface polarization converters naturally have the advantages of low profiles and compatibility with modern integrated devices. A large variety of polarization converters using metasurface technology has been reported on, such as linear polarization rotators [29–32], linear polarization to circular polarization converters [33,34], and other hybrid modes with multiple bands and multiple functions [35,36]. However, only a few works have studied linear-to-dual-circular polarization decomposition metasurfaces [30,31,33], and these functions have not been fully explored yet. Linear-to-dual-circular decomposition is

essential for manipulating electromagnetic waves, as any linearly polarized incident wave may be seen as a combination of a pair of CP waves. Decomposing the two CP components and manipulating them independently may provide a more flexible solution to control the properties of electromagnetic waves. Meanwhile, the metasurface designed based on this principle will still exhibit a stable response performance under large oblique incident waves because the two circularly polarized wave components experience almost the same response during the decomposition of the metasurface.

In this paper, a simple linear-to-dual-circular polarization decomposition metasurface with a single substrate layer operating at 5.7 GHz is proposed. The proposed metasurface unit cell consists of two metallized layers formed by a substrate, where the top layer is a rotated trimming-stubs-loaded circular patch, and the bottom layer is ground. By loading trimming stubs, degenerate modes are introduced in the circular patch for generating CP modes. As a result, the two CP components of the LP incident wave are decomposed. Two methods to add phase gradients to the two CP components to deflect them to different directions are introduced, including adding phase shifters and rotating the structures. Rotating structures will introduce geometric phases that decompose the two CP waves symmetrically without adding any new circuits, while adding phase shifers can break the symmetric limitation of structure rotation at the cost of adding phase shifters at the bottom layer of the proposed structure. The proposed linear-to-dual-circular polarization decomposition metasurface based on structure rotation is analyzed with the help of full-wave simulation by adding two virtual ports on the circular patch and verified by full-wave simulation and experimentation, which provide a flexible and simple solution to manipulate the properties of electromagnetic waves by decomposing the two orthogonal CP modes in LP waves and allowing the editing of them independently. Compared with other reported works, the proposed design exhibits a stable response performance under a wide oblique incidence of up to 50°.

2. General Concept and Metasurface Unit Cell Design

Figure 1 illustrates the general function of the proposed metasurface for linear-to-dual-circular polarization decomposition. The proposed metasurface is a two-layer structure supported by a Rogers 4350 substrate, whose dielectric constant is 3.66, loss tangent is 0.004, and thickness is $h = 1.524$ mm. The top layer of the metasurface is a series of metalized circular patches, whose radius is $r = 7.375$ mm, with the period $d = 26.0$ mm, each of which contains a pair of trimming stubs on its right and left sides with a fixed length $l_s = 1.2$ mm, a fixed width $w_s = 2.0$ mm, and a different rotating angle θ. The bottom layer of the metasurface is a metal ground. All the metal material of this design is copper with a thickness of 0.035 mm and a conductivity of 5.8×10^7 S/m.

When an x-polarized LP planar incident wave, $E_{i,LP}(t)$, impinges on the metasurface, it interacts with each of the metasurface particles and is scattered into a pair of orthogonal CP waves, $E_{r,LHCP}(t)$ and $E_{r,RHCP}(t)$, which are directed to the directions, α_1 and α_2, respectively. Therefore, the LP incident wave is decomposed into a pair of orthogonal CP waves. The detailed design parameters of the metasurface unit cell are listed in the caption of Figure 1.
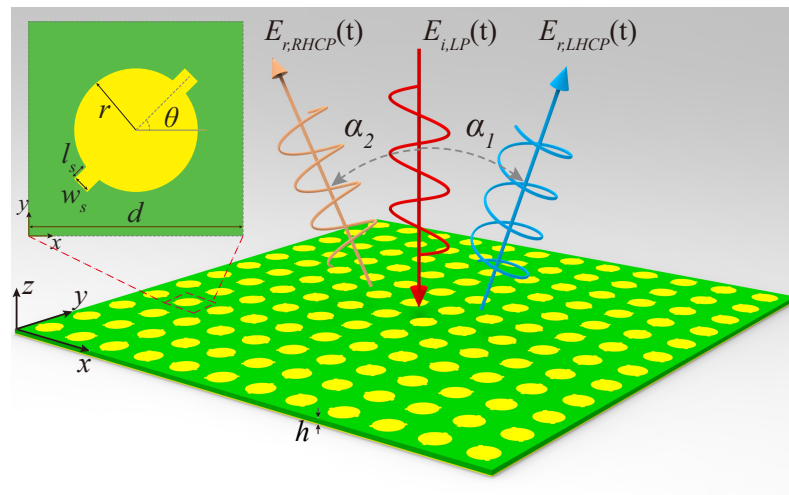
Figure 1. Conceptual illustration of the proposed metasurface for linear-to-dual-circular polarization decomposition. (Design parameters: r = 7.375 mm, w_s = 2.0 mm, l_s = 1.2 mm, d = 26.0 mm, and h = 1.524 mm).

3. Operating Principle and Unit Cell Simulation

It is well known that any LP wave may be seen as a combination of a pair of CP waves. For instance, an x-polarization harmonic wave, $E_{i,LP}(t)$, may be written as

$$
\begin{aligned}
E_{i,LP}(t) &= \sin(\omega_0 t)\boldsymbol{x} \\
&= [\frac{1}{2}\sin(\omega_0 t)\boldsymbol{x} - \frac{1}{2}\cos(\omega_0 t)\boldsymbol{y}] \\
&+ [\frac{1}{2}\sin(\omega_0 t)\boldsymbol{x} + \frac{1}{2}\cos(\omega_0 t)\boldsymbol{y}],
\end{aligned}
\tag{1}
$$

where ω_0 is the angular frequency of the wave, the terms in the first pair of square brackets represent the LHCP wave component, $E_{i,LHCP}(t)$, and the terms in the second pair of square brackets represent the RHCP wave component, $E_{i,RHCP}(t)$.

Assuming that the metasurface particles are able to separate the LHCP and RHCP components from the LP incident wave and add phase gradients $\Delta\beta_1$ and $\Delta\beta_2$ to the LHCP and RHCP components in the x-direction, respectively, the LHCP and RHCP waves reflected by the metasurface $E_{r,LHCP}(t)$ and $E_{r,RHCP}(t)$, are then written as

$$
\begin{aligned}
E_{r,LHCP}(t) &= \frac{1}{N}E_{i,LHCP}(t)\sum_{n=0}^{N-1}e^{-jn(\Delta\beta_1 - 2\pi d\sin\alpha/\lambda_0)}, \\
E_{r,RHCP}(t) &= \frac{1}{N}E_{i,RHCP}(t)\sum_{n=0}^{N-1}e^{-jn(\Delta\beta_2 - 2\pi d\sin\alpha/\lambda_0)},
\end{aligned}
\tag{2}
$$

respectively, where α is the azimuth angle, d is the distance between neighboring metasurface particles, N is the number of metasurface elements along x-direction, and λ_0 is the wavelength of the incident wave at the angular frequency ω_0. Equation (2) shows that the LHCP and RHCP waves are scattered into the directions

$$
\begin{aligned}
\alpha &= \alpha_1 = \arcsin(\frac{\Delta\beta_1\lambda_0}{2\pi d}), \\
\alpha &= \alpha_2 = \arcsin(\frac{\Delta\beta_2\lambda_0}{2\pi d}),
\end{aligned}
\tag{3}
$$

respectively.

A rotated trimming-stub-loaded circular patch is selected as the metasurface unit cell in this paper to separate the dual circular polarization and add phase gradients to the

two CP components. Full-wave simulation is performed to verify these two functions, as shown in Figure 2. Figure 2a shows the full-wave simulation setup, where periodic boundary conditions are applied in both *x*- and *y*- directions of the unit cell. A virtual lumped port, port 1, is added on the circular patch, and a Floquent port 2 is placed on the top of the patch to verify the dual circular polarization separation capability. Two cases with different port 1 positions are studied, respectively, where, in case 1, port 1 is placed on the top half of the circular patch to pick up the RHCP component, whereas, in case 2, port 1 is placed at the bottom half of the circular patch to pick up the LHCP component [37]. Figure 2a plots the scattering parameters of the two cases when $\theta = 0°$. It shows that port 1 receives balanced *x*- and *y*- components ($|S_{2x,1}| = |S_{2y,1}|$) at 5.7 GHz with a $+90°$ phase difference ($\angle S_{2x,1} - \angle S_{2y,1} = 90°$) in case 1, whereas, in case 2, port 1 receives balanced *x*- and *y*- components ($|S_{2x,1}| = |S_{2y,1}|$) at 5.7 GHz with a $-90°$ phase difference ($\angle S_{2x,1} - \angle S_{2y,1} = -90°$), demonstrating that port 1 of the proposed metasurface unit cell can pick up RHCP in case 1 and LHCP in case 2, respectively.
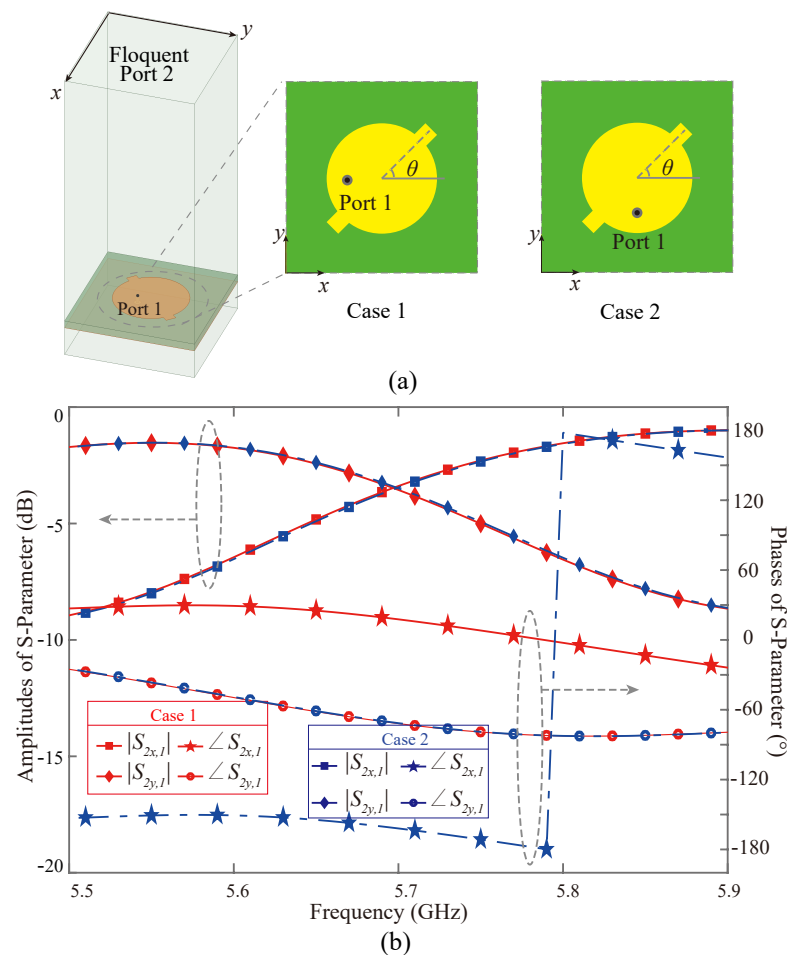
Figure 2. Full-wave simulation results for the linear to dual circular polarization decomposition of the proposed metasurface unit cell. (**a**) Full-wave simulation setup. (**b**) Scattering parameters of the metasurface unit cell with virtual port 1 when $\theta = 0°$.

There are two ways to add the phase gradients to scatter the different CP components to different directions. The most direct way is to connect port 1 to a phase shifter. By shifting different phases at different particles, phase gradients can be added to specified CP components. The other way is to introduce the geometric phases by rotating the particle [38,39]. By rotating the metasurface particle with different angles, θ, different phases can be added to the two CP components. In this work, rotating metasurface particles are chosen to realize the adding phase gradient function with its natural advantages of

passivity, simplicity, and flexibility, compared with adding phase shifters. Figure 3 plots the relationship between the added phase β and the patch rotation angle θ for both cases 1 and 2. Figure 3a plots the relationship for case 1. It shows that as the rotating angle increases from $0°$ to $135°$, port 1 receives the RHCP component ($\angle S_{2y,1} - \angle S_{2x,1} = -90°$ is fixed), whereas the adding phase increases, and the increased phase is the same as the rotating angle. Similarly, Figure 3b plots the relationship for case 2. It shows that port 1 receives the LHCP component ($\angle S_{2y,1} - \angle S_{2x,1} = 90°$ is fixed) as the rotating angle increases from $0°$ to $135°$, whereas the adding phase decreases, and the decreased phase is the same as the rotating angle. If virtual port 1 is removed or stays open, the CP components will be reflected back to a free space with a doubled, added phase. Therefore, by rotating the structure with different angles θ, additional phases with opposite signs $\beta_1 = 2\theta$ and $\beta_2 = -2\theta$ can be added to RHCP and LHCP, respectively.
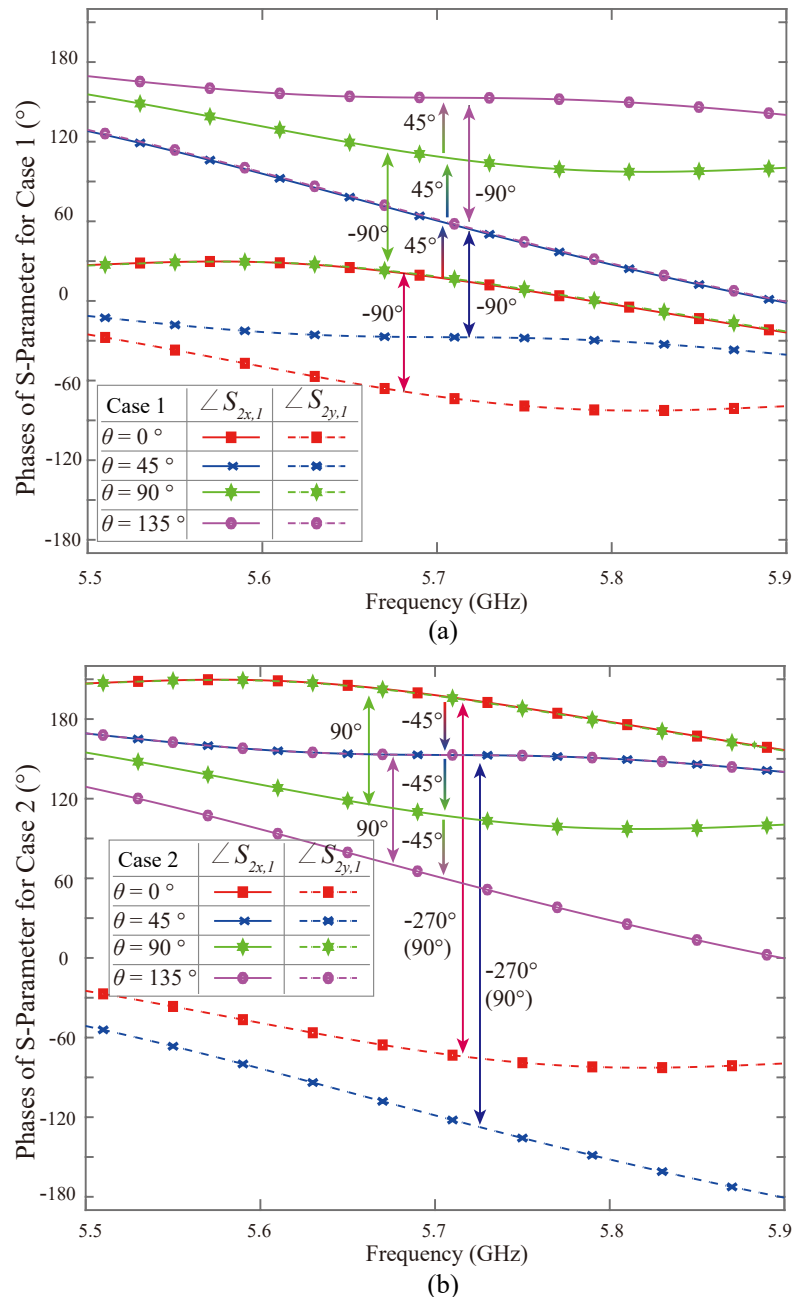
Figure 3. Full-wave simulation results for the relationship between the patch rotating angle θ and the added phases for RHCP and LHCP and β_1 and β_2. (**a**) Case 1. (**b**) Case 2.

Figure 4 depicts the full-wave simulation results for the phase difference ($\angle S_{2y,1} - \angle S_{2x,1}$) under x-polarization incident waves with different oblique angle α for case 1 with $\theta = 90°$. It shows that the proposed metasurface element can decompose the CP components of the LP incident wave stability under a wide oblique incidence of up to $50°$, with the performance, $\angle S_{2y,1} - \angle S_{2x,1} \in [-95° - 85°]$, around 5.7 GHz.
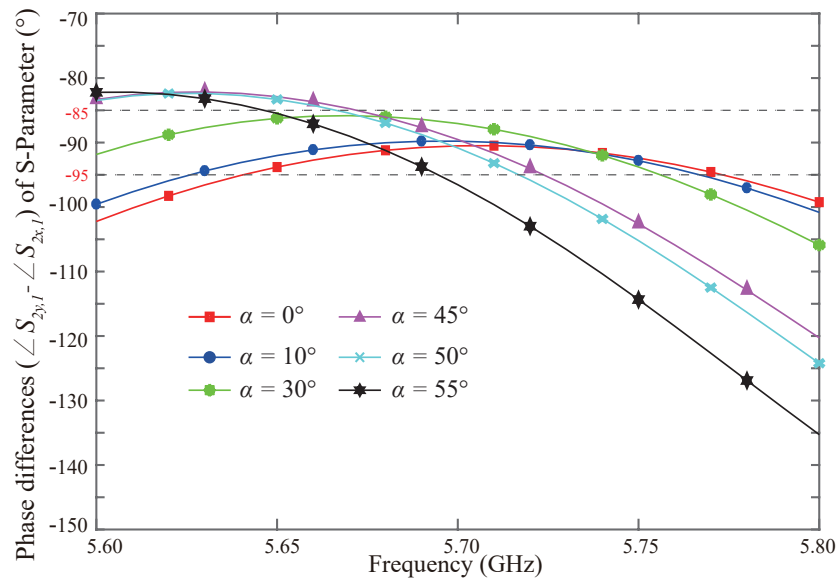

Figure 4. Full-wave simulation results for the phase difference ($\angle S_{2y,1} - \angle S_{2x,1}$) under x-polarization incident waves with different oblique angle α for case 1 with $\theta = 90°$.

4. Full Metasurface Design

A metasurface with 12×12 proposed elements is designed and full-wave simulated. Four element states with different rotating angles, namely, $\theta = 0°, 45°, 90°$, and $135°$, are selected and arranged in sequence along the *x*-direction, as shown in Figure 5, which leads to a $\Delta\beta_1 = 90°$ phase gradient for LHCP and a $\Delta\beta_2 = -90°$ phase gradient for RHCP, respectively, as explained in Figure 3b. Therefore, the scattered LHCP and RHCP beams are directed to $\alpha_1 = 30°$ and $\alpha_2 = -30°$, according to Equation (3).
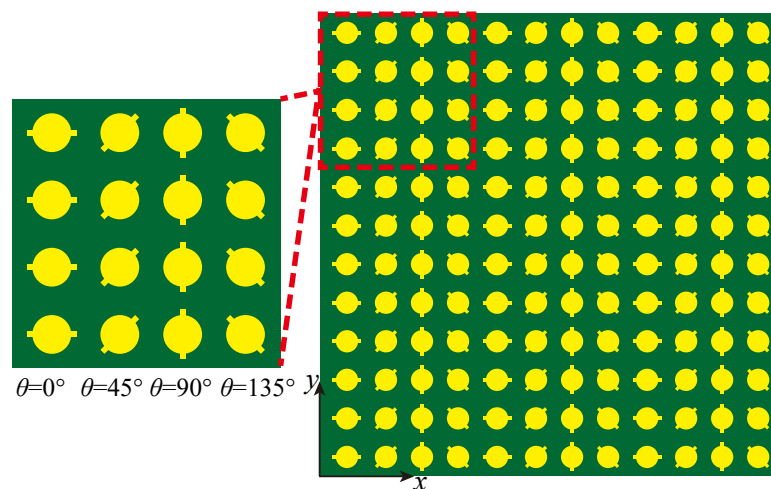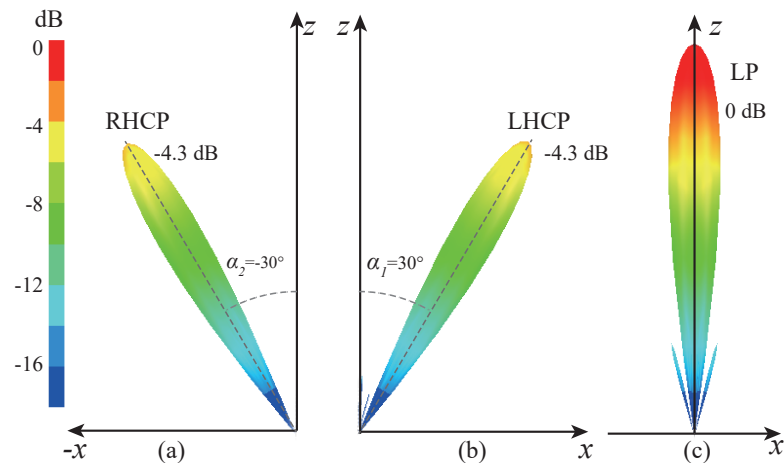

Figure 5. Designed metasurface layout.

Figure 6 plots the comparison of the full-wave simulated scattering beam pattern between the designed metasurface polarization decomposer and a metal plate with the same size at 5.7 GHz under an *x*-polarized incident wave. It clearly shows that the RHCP

(Figure 6a) and LHCP (Figure 6b) beams are scattered to $-30°$ and $30°$, respectively. The 3-dB beamwidth of the two CP waves are about $9.7°$, and the LP-to-CP converting efficiency within the 3-dB beamwidth for each CP wave is approximately 40.1%. This converting efficiency can be further improved by designing a metasurface with a larger aperture. Compared with the scattering beam pattern of the metal plate with the same size as the metasurface in Figure 6c, there is an around 1.3 dB conversion loss, which is mainly introduced by the loss of the dielectric substrate. By changing the rotating angles, θ, in Figure 5, the scattering angles of the CP beams α_1 and α_2 may be tuned, as explained in Section 3.

Figure 6. The full-wave simulated scattering beam pattern of the linear-to-dual circular polarization decomposing metasurface and a metal plate with the same size at 5.7 GHz under *x*-polarized incident wave. (**a**) RHCP scattering beam of the metasurface. (**b**) LHCP scattering beam of the metasurface. (**c**) LP scattering beam of the metal plate.

5. Experimental Demonstration

The designed metasurface, shown in Figure 5, was fabricated and measured in the experiment. Figure 7 shows the measurement setup of the experiment and the photo of the fabricated metasurface prototype. A pair of horn antennas was used as the transmitter and receiver, respectively, and these were placed along an arc track and connected to two ports of a vector network analyzer (VNA). The fabricated metasurface was placed at the center of the arc track and surrounded by absorbing material to avoid undesired scattering waves.
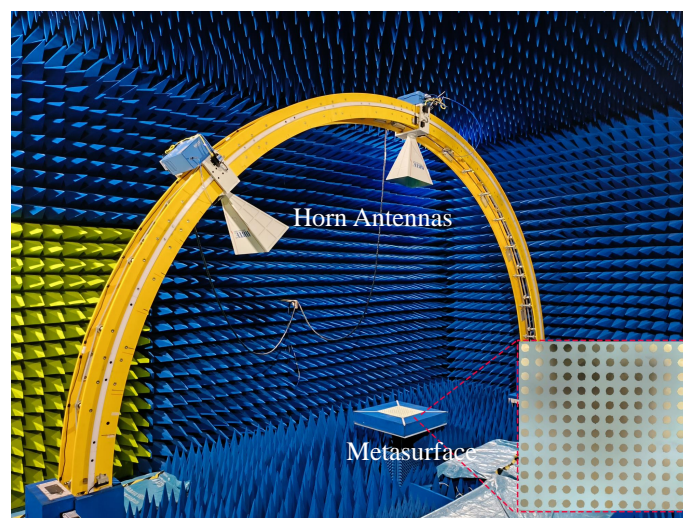
Figure 7. Photo of the experimental setup with the fabricated metasurface prototype.

Figure 8 plots the normalized LHCP and RHCP scattering patterns at 5.7 GHz under an *x*-polarized incident wave for the fabricated metasurface. The measured results show that the RHCP and LHCP beams are scattered to the angles −29.5° and 28.5°, respectively, which are very close to the specified design angles. The measured 3-dB beamwidths of both CP waves are both about 10.1°, and the efficiencies of the LHCP and RHCP waves compared to the power of the total scattered wave are 39.3% and 38.7%, respectively, which are very close to the simulated results The measured axial ratios for the LHCP and RHCP waves at the two directions are 1.58 dB and 1.53 dB, respectively, demonstrating that the proposed metasurface have well decomposed the two CP waves.
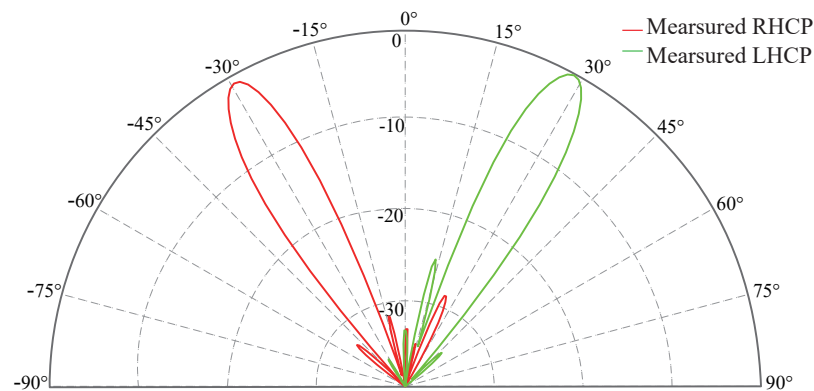
Figure 8. Measured, normalized LHCP and RHCP scattering patterns at 5.7 GHz under *x*-polarized incident wave for the linear-to-dual circular polarization conversion metasurface (Unit: dB).

Finally, Table 1 shows the comparison of features between the proposed work and other reported works. Compared to other reported works, the proposed reflective metasurface can deflect both LHCP and RHCP beams to specified directions simultaneously with only a single substrate layer and relatively thin thickness.

Table 1. Comparison between reported works and this work.

Works	Beam Deflection	Scattered Polarization	Substrate Layers	Substrate Thickness	Metasurface Type	Operating Band
Ref. [33]	Yes	LHCP + RHCP	single	3.00 mm	transmissive	X
Ref. [40]	No	LHCP/RHCP	single	3.50 mm	transmissive	C/X
Ref. [41]	No	LP + LHCP/RHCP	single	6.00 mm	reflective	C
Ref. [42]	No	LHCP/RHCP	double	7.30 mm	reflective	X-K
Ref. [34]	No	LHCP/RHCP	single	0.80 mm	reflective	K_a/V
This work	Yes	LHCP + RHCP	single	1.524 mm	reflective	C

6. Conclusions and Discussion

A novel linear-to-dual-circular polarization metasurface decomposer based on trimming-stub-loaded circular patches was presented in this paper. The polarization decomposition was realized by first decomposing the linear polarization into dual-circular polarization using the trimming-stub-loaded circular patches and then adding different phase gradients to the LHCP and RHCP components by rotating the metasurface particles with different angles. More flexible decompositions, breaking the geometric phase symmetries of the two CP waves, could be realized by adding additional phase shifters at port 1 of Case 1 or 2, shown in Figure 2a, which will be further explored in future works. The proposed metasurface polarization decomposer was theoretically analyzed and demonstrated by both full-wave simulations and experiments. The experimental results agreed well with the simulated ones, which demonstrated the design. The proposed metasurface polarization decomposer may provide a new solution for flexible polarization manipulation.

References

1. Caloz, C.; Achouri, K. *Electromagnetic Metasurfaces: Theory and Applications*, 1st ed.; Wiley: Hoboken, NJ, USA, 2021; p. 1.
2. Holsteen, A.L.; Cihan, A.F.; Brongersma, M.L. Temporal color mixing and dynamic beam shaping with silicon metasurfaces. *Science* **2019**, *365*, 257–260. [CrossRef]
3. Keren-Zur, S.; Avayu, O.; Michaeli, L.; Ellenbogen, T. Nonlinear beam shaping with plasmonic metasurfaces. *ACS Photonics* **2016**, *3*, 117–123. [CrossRef]
4. Jia, X.; Wang, X.; Vahabzadeh, Y. Fast Computation of Resonant Metasurfaces in FDTD Scheme Using Dispersive Surface Susceptibility Model. *IEEE Trans. Antennas Propag.* **2023**, *71*, 713–722. [CrossRef]
5. Wang, X.; Caloz, C. Spread-spectrum selective camouflaging based on time-modulated metasurface. *IEEE Trans. Antennas Propag.* **2020**, *69*, 286–295. [CrossRef]
6. Ramaccia, D.; Sounas, D.L.; Alù, A.; Toscano, A.; Bilotti, F. Phase-induced frequency conversion and Doppler effect with time-modulated metasurfaces. *IEEE Trans. Antennas Propag.* **2019**, *68*, 1607–1617. [CrossRef]
7. Wang, Z.; Zhao, S.; Dong, Y. Pattern Reconfigurable, Low-Profile, Vertically Polarized, ZOR-Metasurface Antenna for 5G Application. *IEEE Trans. Antennas Propag.* **2022**, *70*, 6581–6591. [CrossRef]
8. Zheng, G.; Mühlenbernd, H.; Kenney, M.; Li, G.; Zentgraf, T.; Zhang, S. Metasurface holograms reaching 80% efficiency. *Nat. Nanotechnol.* **2015**, *10*, 308–312. [CrossRef]
9. Huang, L.; Zhang, S.; Zentgraf, T. Metasurface holography: From fundamentals to applications. *Nanophotonics* **2018**, *7*, 1169–1190. [CrossRef]
10. Liu, S.; Yang, D.; Chen, Y.; Sun, K.; Zhang, X.; Xiang, Y. Low-profile broadband metasurface antenna under multimode resonance. *IEEE Antennas Wirel. Propag. Lett.* **2021**, *20*, 1696–1700. [CrossRef]
11. Faenzi, M.; Minatti, G.; González-Ovejero, D.; Caminita, F.; Martini, E.; Della Giovampaola, C.; Maci, S. Metasurface antennas: New models, applications and realizations. *Sci. Rep.* **2019**, *9*, 10178. [CrossRef]
12. Wang, X.; Tong, M.S.; Yang, G.M. Multi-Focus Multi-Null Near-Field Transmitting Focused Metasurface. *IEEE Trans. Antenna Propag.* **2023**, *71*, 3172–3182. [CrossRef]
13. Li, L.; Zhang, P.; Cheng, F.; Chang, M.; Cui, T.J. An Optically Transparent Near-Field Focusing Metasurface. *IEEE Trans. Microw. Theory Tech.* **2021**, *69*, 2015–2027. [CrossRef]
14. Li, M.; Guo, L.; Dong, J.; Yang, H. An ultra-thin chiral metamaterial absorber with high selectivity for LCP and RCP waves. *J. Phys. D Appl. Phys.* **2014**, *47*, 185102. [CrossRef]
15. Deng, T.; Liang, J.; Cai, T.; Wang, C.; Wang, X.; Lou, J.; Du, Z.; Wang, D. Ultra-thin and broadband surface wave meta-absorber. *Opt. Express* **2021**, *29*, 19193–19201. [CrossRef]
16. Caloz, C.; Alù, A.; Tretyakov, S.; Sounas, D.; Achouri, K.; Deck-Léger, Z.L. Electromagnetic nonreciprocity. *Phys. Rev. Appl.* **2018**, *10*, 047001. [CrossRef]
17. Wang, Y.; Chen, W.; Li, X.; Li, S.; Zhou, P. 305–325 GHz Non-Reciprocal Isolator Based on Peak-Control Gain-boosting Magnetless Non-reciprocal Metamaterials. In Proceedings of the 2021 IEEE Radio Frequency Integrated Circuits Symposium (RFIC), Atlanta, GA, USA, 7–9 June 2021; pp. 47–50.
18. Jia, Y.; Liu, Y.; Guo, Y.J.; Li, K.; Gong, S. A dual-patch polarization rotation reflective surface and its application to ultra-wideband RCS reduction. *IEEE Trans. Antennas Propag.* **2017**, *65*, 3291–3295. [CrossRef]
19. Han, J.; Cao, X.; Gao, J.; Wei, J.; Zhao, Y.; Li, S.; Zhang, Z. Broadband radar cross section reduction using dual-circular polarization diffusion metasurface. *IEEE Antennas Wirel. Propag. Lett.* **2018**, *17*, 969–973. [CrossRef]
20. Wang, X.; Yang, G.M. Time-coding spread-spectrum reconfigurable intelligent surface for secure wireless communication: Theory and experiment. *Opt. Express* **2021**, *29*, 32031–32041. [CrossRef]
21. Wang, X.; Caloz, C. Pseudorandom Sequence (Space-) Time-Modulated Metasurfaces: Principles, Operations, and Applications. *IEEE Antennas Propag. Mag.* **2022**, *64*, 135–144. [CrossRef]
22. Zhang, Q.; Pan, W. Countering method for active jamming based on dual-polarization radar seeker. *Int. J. Microw. Wirel. Technol.* **2017**, *9*, 1067–1073. [CrossRef]

23. He, Y.; Zhang, T.; He, H.; Zhang, P.; Yang, J. Polarization Anti-Jamming Interference Analysis with Pulse Accumulation. *IEEE Trans. Signal Process.* **2022**, *70*, 4772–4787. [CrossRef]

24. Rajabalipanah, H.; Rouhi, K.; Abdolali, A.; Iqbal, S.; Zhang, L.; Liu, S. Real-time terahertz meta-cryptography using polarization-multiplexed graphene-based computer-generated holograms. *Nanophotonics* **2020**, *9*, 2861–2877. [CrossRef]

25. Wang, X.; Caloz, C. Phaser-based polarization-dispersive antenna and application to encrypted communication. In Proceedings of the IEEE International Symposium on Antennas and Propagation & USNC/URSI National Radio Science Meeting, San Diego, CA, USA, 9–14 July 2017; pp. 2187–2188.

26. Zhuang, Z.; Suh, S.W.; Patel, J. Polarization controller using nematic liquid crystals. *Opt. Lett.* **1999**, *24*, 694–696. [CrossRef]

27. Ikeda, T.; Sasaki, T.; Ichimura, K. Photochemical switching of polarization in ferroelectric liquid-crystal films. *Nature* **1993**, *361*, 428–430. [CrossRef]

28. Fu, H.; Cohen, R.E. Polarization rotation mechanism for ultrahigh electromechanical response in single-crystal piezoelectrics. *Nature* **2000**, *403*, 281–283. [CrossRef]

29. Khan, M.I.; Fraz, Q.; Tahir, F.A. Ultra-wideband cross polarization conversion metasurface insensitive to incidence angle. *J. Appl. Phys.* **2017**, *121*, 045103. [CrossRef]

30. Wang, X.; Yang, G.M. Linear-polarization metasurface converter with an arbitrary polarization rotating angle. *Opt. Express* **2021**, *29*, 30579–30589. [CrossRef]

31. Zhang, T.; Wang, H.; Peng, C.; Chen, Z.; Wang, X. C-Band Linear Polarization Metasurface Converter with Arbitrary Polarization Rotation Angle Based on Notched Circular Patches. *Crystals* **2022**, *12*, 1646. [CrossRef]

32. Li, J.; Kong, X.; Wang, J.; Miao, Z.; Wang, X.; Shen, X.; Zhao, L. Dual-band polarization-insensitive orbital angular momentum beam generation based on 1-bit polarization-converting transmitting coding metasurface. *Int. J. RF Microw. Comput.-Aided Eng.* **2022**, *32*, e23397. [CrossRef]

33. Li, S.J.; Han, B.W.; Li, Z.Y.; Liu, X.B.; Huang, G.S.; Li, R.Q.; Cao, X.Y. Transmissive coding metasurface with dual-circularly polarized multi-beam. *Opt. Express* **2022**, *30*, 26362–26376. [CrossRef]

34. Liu, X.; Zhou, Y.; Wang, C.; Gan, L.; Yang, X.; Sun, L. Dual-band dual-rotational-direction angular stable linear-to-circular polarization converter. *IEEE Trans. Antennas Propag.* **2022**, *70*, 6054–6059. [CrossRef]

35. Arbabi, A.; Horie, Y.; Bagheri, M.; Faraon, A. Dielectric metasurfaces for complete control of phase and polarization with subwavelength spatial resolution and high transmission. *Nat. Nanotechnol.* **2015**, *10*, 937–943. [CrossRef] [PubMed]

36. Lin, B.Q.; Guo, J.X.; Chu, P.; Huo, W.J.; Xing, Z.; Huang, B.G.; Wu, L. Multiple-band linear-polarization conversion and circular polarization in reflection mode using a symmetric anisotropic metasurface. *Phys. Rev. Appl.* **2018**, *9*, 024038. [CrossRef]

37. Balanis, C.A. *Antenna Theory: Analysis and Design*, 4th ed.; Wiley: Hoboken, NJ, USA, 2015.

38. Berry, M.V. Quantal phase factors accompanying adiabatic changes. *Proc. R. Soc. Lond. A* **1984**, *392*, 45–57.

39. Pancharatnam, S. Generalized theory of interference and its applications. *Proc. Indian Acad. Sci.-Sect. A* **1956**, *44*, 398–417. [CrossRef]

40. Li, Z.Y.; Li, S.J.; Han, B.W.; Huang, G.S.; Guo, Z.X.; Cao, X.Y. Quad-band transmissive metasurface with linear to dual-circular polarization conversion simultaneously. *Adv. Theory Simul.* **2021**, *4*, 2100117. [CrossRef]

41. Gao, X.; Yang, W.L.; Ma, H.F.; Cheng, Q.; Yu, X.H.; Cui, T.J. A reconfigurable broadband polarization converter based on an active metasurface. *IEEE Trans. Antennas Propag.* **2018**, *66*, 6086–6095. [CrossRef]

42. Lin, B.; Lv, L.; Guo, J.; Liu, Z.; Ji, X.; Wu, J. An ultra-wideband reflective linear-to-circular polarization converter based on anisotropic metasurface. *IEEE Access* **2020**, *8*, 82732–82740. [CrossRef]